

PDF hosted at the Radboud Repository of the Radboud University Nijmegen

The version of the following full text has not yet been defined or was untraceable and may differ from the publisher's version.

For additional information about this publication click this link.

<http://hdl.handle.net/2066/34682>

Please be advised that this information was generated on 2018-07-07 and may be subject to change.

How to hide large scale outflows: size constraints on the jets of Sgr A*

Sera Markoff^{1*}, Geoffrey C. Bower² and Heino Falcke³

¹*Astronomical Institute “Anton Pannekoek”, University of Amsterdam, Kruislaan 403, 1098SJ Amsterdam, the Netherlands*

²*601 Campbell Hall, Astronomy Department & Radio Astronomy Lab, Berkeley, CA 94720, USA*

³*Department of Astrophysics, Radboud University, Postbus 9010, 6500GL Nijmegen; ASTRON, Postbus 2, 7990AA Dwingeloo, the Netherlands*

ABSTRACT

Despite significant strides made towards understanding accretion, outflow, and emission processes in the Galactic Center supermassive black hole Sagittarius A*, the presence of jets has neither been rejected nor proven. We investigate here whether the combined spectral and morphological properties of the source at radio through near infrared wavelengths are consistent with the predictions for inhomogeneous jets. In particular, we construct images of jets at a wavelength of 7mm based on models that are consistent with the spectrum of Sgr A*. We then compare these models through closure quantities with data obtained from the Very Long Baseline Array at 7mm. We find that the best-fit jet models give comparable or better fits than best-fit Gaussian models for the intrinsic source found in previous analyses. The best fitting jet models are bipolar, are highly inclined to the line of sight ($\theta \gtrsim 75^\circ$), may favor a position angle on the sky of 105° , and have compact bases with sizes of a few gravitational radii.

Key words: galaxies: jets — galaxies: active — black hole physics — Galaxy: nucleus — radiation mechanisms: non-thermal

1 INTRODUCTION

Sgr A* is the compact radio source in our Galactic center, originally discovered over 30 years ago by Balick & Brown (1974). Years of dedicated observations of stellar orbits (e.g., Ghez et al. 2000; Schödel et al. 2003) and precise, high-resolution radio astrometry (Backer & Sramek 1999; Reid et al. 2003) have led to Sgr A* being unambiguously associated with the central supermassive black hole. Most recently, the first measurements of the intrinsic size of Sgr A* have been achieved Bower et al. (2004); Shen et al. (2005); Bower et al. (2006), giving information about spatial structures extremely close to the black hole.

For many years Sgr A* was only known to emit in the radio bands, with a flat/inverted spectrum fairly typical of the compact cores of other nearby low-luminosity galaxies (e.g. Ho 1999; Nagar et al. 2002). However, the absence of infrared and higher energy emission was puzzling given that at least some nonthermal accretion activity would be expected for a source that is powered by weak accretion. The first positive identification of Sgr A* in the X-ray band with the *Chandra Observatory* did not immediately settle the issue (Baganoff et al. 2001, 2003). The dominant quies-

cent emission turned out to be extended and nonvariable, and thus likely associated with hot gas within the Bondi capture radius of the black hole (Quataert 2002). In contrast, the approximately daily flares of nonthermal X-ray emission discovered later seem to originate within tens of $r_g = GM/c^2$ from the black hole itself. Since this discovery, Sgr A* has also been identified in the near infrared (NIR), where it shows correlated variability with the X-ray band on similar timescales (Genzel et al. 2003; Ghez et al. 2004; Eckart et al. 2004). While this suggests a low-level of active galactic nuclei (AGN)-like behavior, the luminosity of Sgr A* ($\sim 10^{-9} L_{\text{Edd}}$) is weak enough to raise questions about comparisons with more luminous accreting black holes.

Several models have been developed over the years to explain the broadband emission of Sgr A*, ranging from Bondi-Hoyle infall (Melia 1992), to various radiatively-inefficient accretion flows (RIAFs; Narayan et al. 1998; Yuan et al. 2003), to jets (Falcke & Biermann 1995; Falcke & Markoff 2000; Markoff et al. 2001), and combinations thereof (Yuan et al. 2002). The persistence of such a wide range of models can be attributed to some extent to the lack of constraints on the nonthermal part of the X-ray spectrum. Fitting the most compact “submm bump” region of the spectrum results in fairly similar internal parameters for all current models, and this “theoretical degeneracy” cannot easily be broken without better morphological information

* E-mail: sera@science.uva.nl; gbower@astro.berkeley.edu; falcke@astron.nl

from Very Large Baseline Interferometry (VLBI). Unfortunately with current sensitivity and resolution limits, most structure in the source is washed out by a strong scattering medium in the central Galactic regions (see, e.g. Bower et al. 2006).

Recently, however, several new observational techniques have been developed which may help discern between various models. For instance, the stringent limits placed on the accretion rate ($\dot{M} \sim 10^{-9} - 10^{-7} M_{\odot}/\text{yr}$) by measurements of linear polarization (Aitken et al. 2000; Bower et al. 2003, 2005; Marrone et al. 2006b; Macquart et al. 2006) have ruled out classical versions of the Bondi-Hoyle and Advection-Dominated Accretion Flow (ADAF) models. Similarly, better determinations of the frequency-dependence of the electron scattering law in the Galactic center (GC) (Bower et al. 2004; Shen et al. 2005; Bower et al. 2006) have resulted in new constraints on models via their size-versus-frequency predictions. While the different groups have found the index of the size-versus-frequency relation to range from $\sim 1 - 1.6$, clearly any successful model must be stratified (optically thick and thus having a photosphere whose observable size varies with frequency) to achieve this. The determination of the scattering law to a high degree of accuracy has allowed, for the first time, a dependable measurement of the intrinsic size of Sgr A* along one axis as a function of frequency. This breakthrough, along with the expectation of eventually determining the size in the other axis, means we are finally at a key point where differences between models can be empirically tested.

In this paper, we use both the spectral data in combination with the new VLBI measurements of the source photosphere at 43 GHz (from Bower et al. 2004 plus one new observation, see below) in order to place new constraints on jet models. In Section 2, we expand on the motivations for this project, in Section 3 we introduce the model, in Section 4 we explain the methodology and summarize our results in Section 5, and discuss our conclusions in Section 6.

2 THE EVIDENCE FOR JETS IN SGR A*

Because no jet in Sgr A* has yet been directly imaged, it is important to first discuss the evidence in favor of jets in Sgr A*. The lack of a resolved core/jet structure is not surprising given the low luminosity of Sgr A*, which suggests a small angular size for the jet, and the scattering screen in our line of sight towards Sgr A*, which obscures small structures. Previous modeling of the structure of Sgr A* has succeeded in separating the intrinsic and scatter-broadened images of Sgr A* via a Gaussian parameterization of the intrinsic size. A primary goal of this paper is to go beyond this simple parameterization.

In fact, there are several strong arguments for jets in Sgr A*. On a purely theoretical level, some form of jet production seems to go hand-in-hand with accretion around black holes, both at the galactic as well as stellar scales. In stellar black holes accreting from a binary companion, or X-ray binaries (XRBs), jet production is observed to be cyclic over outburst cycles. The strongest (relative to the system energetics) and steadiest jets occur during the low-luminosity state, called the Low/Hard State, while dur-

ing the highest luminosity state, the jets appear quenched (Fender et al. 1999). The low-luminosity jets are compact and self-absorbed with a flat/inverted spectrum, and correlated radio/X-ray variability has demonstrated that the jets increasingly dominate the power output as the luminosity decreases (Fender et al. 2003). The weakest accreting black hole we can study with reasonable statistics besides Sgr A* is the XRB A0620-00, in which radio emission has recently been detected (Gallo et al. 2006). At an X-ray luminosity of $\lesssim 5 \times 10^{-9} L_{\text{Edd}}$, very close to that of Sgr A*, efficient jets are still produced in this black hole, with characteristics matching those at higher powers. If general relativity's basic prediction of scaling black hole physics holds, this is a strong argument for jet production in Sgr A*.

The radio spectrum, radio variability, and high-frequency linear polarization are all similar to other nearby low-luminosity AGN (LLAGN; Ho 1999; Falcke & Biermann 1999; Bower et al. 2002; Nagar et al. 2002, 2005). Most of the observed cores are accretion-powered, and have the signature flat/inverted, self-absorbed radio spectrum associated with compact jets (Blandford & Königl 1979). While the jets can only generally be resolved in the brightest sources, when they are resolved they dominate the unresolved core by at least a factor of a few. The results of these surveys strengthen the arguments for a jet in Sgr A* based on its radio spectrum and polarization.

One source that is particularly interesting because of its many parallels with Sgr A* is the nucleus of the nearby LLAGN M81. M81* is our nearest LLAGN besides Sgr A*, and resides in the same kind of spiral galaxy as the Milky Way. Its mass has been derived from line spectroscopy (using *HST*; Devereux et al. 2003) to be $7 \times 10^7 M_{\odot}$, only ~ 30 times the mass of Sgr A*. M81* also possesses the typical compact flat/inverted core spectrum (Falcke 1996; Markoff et al., in prep.) and, more importantly, the same high levels of circular rather than linear polarization in the centimeter radio band as Sgr A* (Brunthaler et al. 2001, 2006).

The M81* jet is one-sided, very small (700-3600 AU depending on the frequency, with a roughly $\sim 1/\nu$ dependence), and exhibits occasional bends in its morphology (Bietenholz et al. 2000). Scaling the size by mass alone would argue for a $\sim 20 - 120$ AU jet in Sgr A*, but the observed size should also scale with luminosity, depending on the particulars of the jet model and frequency. In fact, the jet nature of M81* was difficult to establish due to the high level of compactness. Taking into account Sgr A*'s five orders of magnitude lower power, as well as the scattering screen, it is not surprising that no jet has yet been detected in our Galactic center.

Another argument in favor of jets comes from the recent detection of short time delays of about 0.5-1 hr between 43 and 22 GHz for waves of variability traveling from high to low frequencies (Yusef-Zadeh et al. 2006). This variability is fully consistent with outflowing, adiabatically expanding blobs of plasma, as would be expected for jets (in fact, the model the authors use to interpret their results was developed in this context).

Finally, the recent size-versus-frequency scaling detections support an optically thick, stratified model such as a self-absorbed jet. While the predictions of the jet model presented in Falcke & Markoff (2000), as well as that of RIAFs (Yuan et al. 2006), are consistent with a $1/\nu$ scal-

ing, and thus with the results in Bower et al. (2004) and Shen et al. (2005), they disagree with the steeper index determined more recently by Bower et al. (2006). If this latter result is indeed correct, it suggests that the current versions of all models, jets included, need to be modified to show a stronger dependence on observing frequency. Because this issue is still under debate, however, in this paper we are still using the original scaling relation.

Although the circumstantial evidence is significant, there are other complications which could argue against jets. For instance, XRBs in their steady-jet producing Low/Hard state display a correlation between their radio and X-ray luminosities that holds over at least seven orders of magnitude in luminosity (Corbel et al. 2003; Gallo et al. 2003). Among other things, this correlation can be used as a gauge for “typical” levels of activity. The recent radio detection of A0620-00 falls exactly on the correlation, extending it to even lower luminosities and indicating that the same mechanism is at work as in brighter sources where jets can be imaged. If the physics driving the correlation scales in a predictable way with mass, it should apply to LLAGN as well, where the mass enters mainly as a normalization factor for the same correlation slope. This relationship between radio and X-ray luminosities and mass is called “the fundamental plane of black hole accretion” and has been explored in several recent papers (Merloni et al. 2003; Falcke et al. 2004; Kording et al. 2006; Merloni et al. 2006). When Sgr A* in quiescence is placed on this plane, it falls well below the correlation in predicted X-rays, given its radio luminosity. One could interpret this as the complete dominance of the jet over inflow processes at the lowest of luminosities, but it could also mean that the emission mechanisms themselves have undergone a transition to a different mode of emission entirely.

In order to try to cast new light on these long-standing ambiguities and place more stringent constraints on the possible presence of jets in Sgr A*, we have developed a new method to combine spectral and morphological data. Our results will set the stage for future tests with upcoming VLBI observations at millimeter and submillimeter wavelengths, where the morphology is less affected by scattering and resolution is comparable to a few r_g .

3 MODEL

Like most models involving optically thick, collimated outflows, we build on the initial work of Blandford & Königl (1979). These authors demonstrated the “conspiracy” of how a perfectly flat spectrum ($\alpha \sim 0$, $F_\nu \propto \nu^{-\alpha}$) can result from a superposition of self-absorbed contributions along a conical, idealized jet. When more realistic physics such as bulk acceleration, full particle distributions and cooling are included, compact jets show a slight spectral inversion in the radio wavebands, with $\alpha \sim 0.0 - 0.2$. The model used here is based on a model developed for Sgr A* (Falcke & Markoff 2000), which has been significantly modified to extend to XRBs and LLAGN in general. For a detailed description see the appendix in Markoff et al. (2005); we provide only a brief summary below.

The model is based upon four assumptions: 1) the total power in the jets scales with the total accretion power at

the innermost part of the accretion disk, $\dot{M}c^2$, 2) the jets are freely expanding and only weakly accelerated via their own internal pressure gradients, 3) the jets contain cold protons which carry most of the kinetic energy while leptons dominate the radiation and 4) particles have the opportunity to be accelerated into power-law tails. In sources accreting at higher levels this latter point would be more important, but as we will show later, there is not much capacity in the Sgr A* spectrum for significant particle acceleration.

The base of the jets consist of a small nozzle of constant radius where no bulk acceleration occurs. The nozzle absorbs our uncertainties about the exact nature of the relationship between the accretion flow and the jets, and fixes the initial value of most parameters. Beyond the nozzle the jet expands laterally with its initial proper sound speed for a relativistic electron/proton plasma, $\gamma_s \beta_s c \sim 0.4c$. The plasma is weakly accelerated by the resulting longitudinal pressure gradient force, allowing an exact solution for the velocity profile via the Euler equation (see, e.g., Falcke 1996). This results in a roughly logarithmic dependence of velocity upon distance from the nozzle, z . The velocity eventually saturates at large distances at Lorentz factors of $\Gamma_j \gtrsim 2-3$. The size of the base of the jet, r_0 , is a free parameter (but expected to fall within several r_g) and once fixed determines the radius as a function of distance along the jet, $r(z)$. There is no radial dependence in this model.

The model is most sensitive to the fitted parameter N_j , which acts as a normalization. It dictates the power initially divided between the particles and magnetic field at the base of the jet, and is expressed in terms of a fraction of the Eddington luminosity $L_{\text{Edd}} = 1.25 \times 10^{38} M_{\text{bh},\odot} \text{ erg s}^{-1}$. Once N_j and r_0 are specified and conservation is assumed, the macroscopic physical parameters along the jet are determined. We assume that the jet power is roughly shared between the internal and external pressures. The radiating particles enter the base of the jet where the bulk velocities are lowest, with a quasi-thermal distribution. In higher power jets, a significant fraction of the particles are accelerated into a power-law tail, however in Sgr A* this seems to be less of an effect. The particles in the jet radiatively cool via adiabatic expansion, the synchrotron process, and inverse Compton upscattering; however, adiabatic expansion is assumed to dominate the observed effects of cooling. Because Sgr A* has no “standard thin accretion disk” (e.g. Shakura & Sunyaev 1973), nor even a fossil disk, which would be apparent in the infrared (Falcke & Melia 1997), the photon field for inverse Compton upscattering is entirely dominated by locally produced synchrotron photons. Fig. 1 shows an example of the resulting broadband spectrum plotted against the data for Sgr A*.

Besides those mentioned above, the other main fitted parameters are the ratio of length of the nozzle to its radius h_0 , the electron temperature T_e , the inclination angle between the jet axis and line of sight θ_i and the equipartition parameter between the magnetic field and the radiating (lepton) particle energy densities, k .

Aside from Sgr A*, this class of model has been successfully applied to several LHS XRBs (Markoff et al. 2001, 2003; Markoff et al. 2005; Migliari et al. 2007; Gallo et al., in prep.) and other LLAGN (Yuan et al. 2002; Filho et al., in prep., Markoff et al., in prep.). As would be expected from the existence of the fundamental plane, all significantly sub-

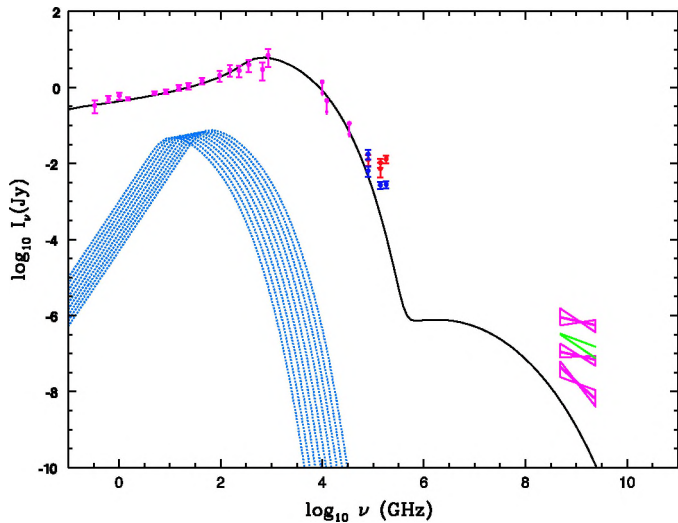


Figure 1. The broadband data set for Sgr A* used to constrain our models, taken from the average spectrum up until the sub-millimeter (Melia & Falcke 2001), with additional low frequency points from Nord et al. (2004) and Roy & Pramesh Rao (2004) and infrared data from Genzel et al. (2003) and Ghez et al. (2004). The X-ray “bow-ties” represent the quiescent (lowest), average daily *Chandra* flare (middle) and brightest *Chandra* (top) power-laws with errors indicated (Baganoff et al. 2001; Baganoff 2003). The “V” shape indicates the two *XMM-Newton* flares presented in Bélanger et al. (2005). The solid curve shows a representative quiescent model with synchrotron and synchrotron self-Compton peaks. The dotted lines illustrate the contribution of the quasi-thermal particles from each increment along the jet, which superimpose to give the characteristic flat/inverted synchrotron spectrum.

Eddington accreting black holes do seem to share some basic underlying physics across the mass scale. However, as mentioned above, Sgr A* does not participate in the radio/X-ray correlation and can only be reconciled into this picture if significant particle acceleration is lacking. This is a very interesting point, because the appearance (or non-appearance) of a jet is strongly dependent on its internal particle distributions. A power-law tail of accelerated particles results in more optically thin synchrotron emission over a broader frequency range from each jet increment. Thus when observing at a single frequency, a larger range of increments are able to contribute to the profile, resulting in a larger jet image, as we show in Fig. 2.

4 METHODOLOGY

4.1 Modeling the spectral data of Sgr A*

In order to break the current degeneracy based on modeling the spectral data alone, we are for the first time calculating the predicted size and morphology of jet models which give a good description of the broadband data. After convolving these “maps” with the scattering screen, we then compare the results to closure quantities from VLBI, which provide information about the structure. The model predictions are analyzed in the same way as the observations.

The 41 models presented here were chosen to represent a range which samples the full parameter space within the

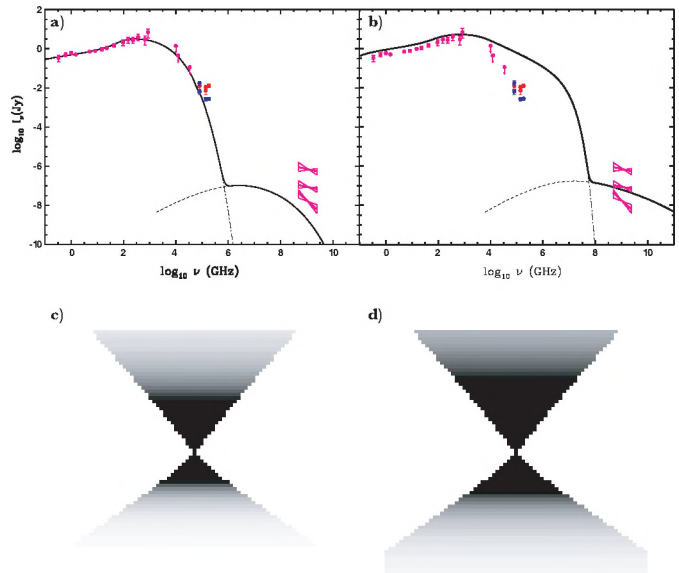


Figure 2. Illustration of the effect of particle acceleration on the observed jet profile. Panel a) shows the quiescent model 3, which provides the best statistical description of the radio data. Panel b) shows a model with the exact same parameters except for the addition of significant particle acceleration, where 75% of the particles in the quasi-thermal distribution are accelerated into a power-law with energy index 2.2, and a cutoff 50 times higher than the minimum energy (which is fixed to the peak of the thermal distribution). Panels c) and d) show the profile this model produces on the sky, prior to convolution with the scattering Gaussian. The scale of the images is 1 mas. The images are saturated to emphasize the brightest (darkest) parts of the jets. A tail of accelerated particles serves to significantly lengthen the jets profile at a given frequency.

constraints of a reasonably good ($\chi^2 < 1$) description of the radio through IR. For quiescent models, they are further constrained to fall within a factor of a few under the X-ray quiescent limits from *Chandra*. Flaring models are those which can account for either the average daily flaring flux or the highest detected with *Chandra* in the X-ray band, via some form of heating, accelerating or increased power compared to the quiescent state. We initially conducted a very rough search of a large region of parameter space for the first 20 models, then focused on a smaller region to explore properties nearest the best-fitting models, as well as for flares. A systematic exploration of the parameter space would be at least a 6 dimensional parameter cube, which we deemed too computationally intensive for this initial test study.

Because there is still significant uncertainty about what to consider the “quiescent” versus “flared” IR flux amplitude and slope, we did not include the IR in the χ^2 calculation but rather required the model to fall reasonably within range of the errors. The inability to constrain the exact IR and X-ray quiescent flux accounts for almost all of the allowed range in the fitted parameters for the quiescent state, otherwise the parameters would be fairly tightly determined. In this way the addition of morphological fitting can constrain the quiescent contribution above the submm band. We also compared our models to the simultaneous radio through IR data set presented in An et al. (2005), and found the level

agreement between the two data sets so good that we did not feel it provided an additional constraint. One of our secondary goals was to explore observable differences in the photosphere during flaring states.

Table 1 lists the models and their parameters, along with relevant comments.

Table 1. Jet model parameters

Model	Q/F	N_j ($10^{-7} L_{\text{Edd}}$)	r_0 (r_g)	h_0/r_0	θ_i ($^\circ$)	T_e (10^{11} K)	k	$n_e = n_p$	n_j	Other ^a	χ^2/DoF^b
1	Q	3.6	5	2.5	51	2.2	10	y	2		5.77/9
2	Q	6.2	5	1.5	67	1.9	10	y	2		8.48/9
3	Q	7.2	5	1.1	75	1.8	15	y	2		4.73/9
4	Q	5.8	3	1.3	55	1.8	10	y	2		7.05/9
5	Q	6.6	3	1.2	52	1.7	10	y	2		4.98/9
6	Q	6.0	3.5	1.2	45	1.7	10	y	2	$\beta(z)$ stretched	4.74/9
7	Q	10	5	1.2	65	2.4	2	y	2	$\beta(z)$ stretched	6.38/9
8	Q	7.2	3.5	1.7	57	1.6	10	y	1		4.88/9
9	Q	2.6	3.5	2.2	50	2.0	10	n	2		5.76/9
10	Q	1.8	3.5	1.9	50	2.1	4	n	2		5.27/9
11	Q	3.0	3.5	2.4	50	1.7	10	n	1		6.69/9
12	Q	6.6	5	1.1	69	2.0	10	y	2		5.54/9
13	Q	3.4	8	1.4	63	2.0	30	y	2		9.44/9
14	Q	2.4	5	1.8	55	2.1	6	n	2		5.67/9
15	F	16	5	1.3	67	7.0	0.1	y	2		13.22/9
16	F	16	5	1.1	75	7.2	0.1	y	2	Av. Chandra flare, SSC	10.06/9
17	F	18	5	1.1	75	7.9	0.05	y	2	Av. Chandra flare, SSC	14.31/9
18	Q	7.2	5	1.1	85	1.9	15	y	2		5.68/9
19	F	18.4	5	1.1	85	6.5	0.09	y	2	Av. Chandra flare, SSC	10.15/9
20	Q	11	3.5	1.0	85	1.4	15	y	2		6.44/9
21	Q	7.6	3.5	1.0	85	1.4	15	n	2		5.69/9
22	Q	14	5	1.0	85	1.5	15	y	1		9.15/9
23	Q	10	3	1.0	85	1.5	15	y	2		8.69/9
24	Q	19	2.5	1.0	85	1.0	15	y	2		12.19/9
25	Q	20	2	1.0	70	0.8	20	y	2		12.66/9
26	Q	19	2	1.0	80	1.0	15	y	2		11.67/9
27	Q	13	3	0.6	87	1.3	15	y	2		5.46/9
28	Q	13	3	0.6	87	1.3	15	y	2	$z_{\text{acc}} = 50, p = 3, u/f = 7 \times 10^{-3}, \text{plf} = 0.1$	4.51/5
29	Q	13	3	0.6	87	1.3	15	y	2	$z_{\text{acc}} = 50, p = 3, u/f = 3 \times 10^{-4}, \text{plf} = 0.1$	4.52/5
30	Q	140	5	0.6	85	0.3	15	y	2	PL: $p = 3.4, \gamma_{e,\text{max}} = 2 \times 10^3$	7.10/7
31	Q	38	3	0.6	85	0.7	15	y	2	PL: $p = 3.4, \gamma_{e,\text{max}} = 3 \times 10^3$	8.23/7
32	Q	60	3	0.4	85	0.6	15	y	2	PL: $p = 3.8, \gamma_{e,\text{max}} = 2.5 \times 10^3$	3.83/7
33	Q	23	2	0.7	85	0.95	15	y	2		5.99/9
34	F	19	2.5	1.0	85	1.0	15	y	2	$z_{\text{acc}} = 10, p = 1.7, u/f = 0.014, \text{plf} = 1 \times 10^{-4}$ Biggest Chandra flare, synch.	10.35/5
35	F	11.5	2.5	0.95	85	1.0	50	y	2	$z_{\text{acc}} = 10, p = 1.6, u/f = 0.014, \text{plf} = 6 \times 10^{-6}$ Av. Chandra flare, synch.	5.90/5
36	F	50	2.5	1.0	85	5.0	0.01	y	2	PL: $p = 2.3, \gamma_{e,\text{max}} = 500$ Biggest Chandra flare, SSC	4.512/7
37	Q	50	2.5	1.0	85	1.3	1	y	2	$z_{\text{acc}} = 5, p = 1.2, u/f = 3 \times 10^{-7}, \text{plf} = 3 \times 10^{-3}$	14.65/5
38	F	16	3	1.0	85	0.6	2	y	2	PL: $p = 1.01, \gamma_{e,\text{max}} = 220$ $z_{\text{acc}} = 5, p = 1.01, u/f = 3 \times 10^{-7}, \text{plf} = 5 \times 10^{-4}$ Av. Chandra flare, SSC	4.45/4
39	F	16	3	1.0	85	0.6	2	y	2	PL: $p = 1.01, \gamma_{e,\text{max}} = 220$ Av. Chandra flare, SSC	4.04/7
40	F	80	3	1.01	85	0.6	0.1	y	2	PL: $p = 1.5, \gamma_{e,\text{max}} = 500$ Biggest Chandra flare, SSC	112/7
41	F	25	2.5	1.01	85	2.0	1	y	2	$z_{\text{acc}} = 5, p = 2.7, u/f = 3 \times 10^{-3}, \text{plf} = 0.04$ Steep XMM flare, synch.	4.193/5

Note. — ^a This column describes other adaptations to the standard model. “ β stretched” means that we increased the velocity as a function of distance along the jet by a factor depending on that distance. The other comments refer to various ways of accelerating particles in the jets. For rows with four additional parameters, z_{acc} is the location of the acceleration region, p is the particle index, u/f are plasma parameters which determine the rate of acceleration, and plf is the fraction of particles accelerated out of the original quasi-thermal distribution (see Appendix in Markoff et al. 2005 for details). For rows with two additional parameters, the particles are assumed to be accelerated already in the nozzle, in a power law with $\gamma_{e,\text{min}}$ corresponding to the input temperature, particle index p and maximum lepton Lorentz factor $\gamma_{e,\text{max}}$.

^b The χ^2 statistic is sensible for quiescent models only, since it is calculated using an averaged quiescent spectrum. We include the value for flare models just as a reference.

4.2 Analysis Technique

The jet emission is calculated along its length in increments. In order to determine the appearance of the jet on the sky, we calculate the contribution to the synchrotron spectrum at 43 GHz from each increment, assumed to be evenly distributed over the radius and increment width. Relativistic angle aberration (e.g. Lind & Blandford 1985) for the increments' bulk Lorentz factors is taken into account. This "profile" is then fed into an IDL routine which creates a FITS image of the jet. Each model was then rotated by position angles in steps of 15 degrees covering the full range of angle. Furthermore, once the jet was placed with the specified rotation on the image, we convolved it with a Gaussian ellipse of the scattering as determined below.

Jet models were imaged on a 2001×2001 grid with a pixel resolution of $14 \mu\text{arcsec}$. Fig. 3 shows the underlying jet model and the resulting scatter-broadened model in linear and logarithmic scales. The large-scale differences seen in the logarithmic representation do not make a significant contribution to our ability to differentiate between these models, since the total flux density in the outer regions is very small.

We directly compare the jet models with high resolution data obtained at a wavelength of 43 GHz (7 mm). The data are obtained primarily with the Very Long Baseline Array (VLBA) and in some cases include a single Very Large Array (VLA) antenna. Eight epochs of observations are described in Bower et al. (2004). In addition, we include new observations obtained with the VLBA and the 100m Green Bank Telescope on 18 May 2004 (experiment code BB183). These observations were reduced in the same method as the earlier epochs with calibration for single-band delay and multi-band delay and rate.

We construct closure amplitude and closure phase from the visibility data. The closure phase is the sum of interferometric phases for a triangle of baselines. The closure amplitude is a product of interferometric amplitudes for baseline quadrilaterals. Analysis of the closure quantities is less sensitive than the analysis of calibrated visibilities because of the reduced number of degrees of freedom. The closure quantities are independent of amplitude and phase calibration, however. This property which makes them valuable estimators of source structure that are unbiased by systematic errors in calibration.

In Bower et al. (2004) elliptical Gaussian models were fitted to the closure amplitudes for data sets at wavelengths from 7 mm to 6 cm. This fitting produced a best-fit elliptical Gaussian as a function of wavelength. Combining the VLBI measurements with new measurements of the size at wavelengths between 17 and 24 cm based on VLA observations, a size-wavelength relation was determined (Bower et al. 2006). The scattering ellipse from the long wavelength observations was computed to be $1.31 \times 0.64 \text{ mas cm}^{-2}$ in position angle 78° . The size of the ellipse scales as the wavelength-squared. Deviations from the wavelength-squared law at short wavelengths are indicative of the intrinsic size becoming comparable to the scattering size. The magnitude of the scattering ellipse is determined by the spectrum of turbulent electron density fluctuations. The orientation and axial ratio of the scattering ellipse are determined by the magnetic field properties of the plasma in which the scattering originates.

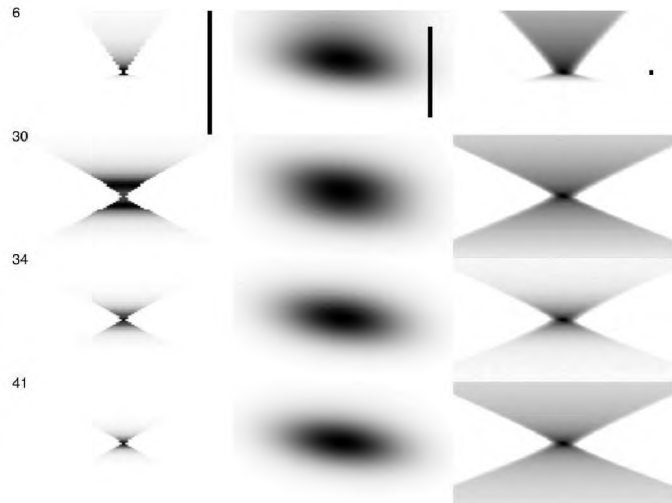


Figure 3. Images of models 6, 30, 34, and 41. In the left column, we show the jet model with a linear stretch. In the middle column, we show the jet model after it has been convolved with the elliptical Gaussian representing scattering, also with a linear stretch. In the right column, we show the convolved jet model in a logarithmic stretch. The scale bars in the top row indicate 1 milli-arcsecond.

Each model was directly compared with closure quantities from the data. First, we added a noise bias to each model image equal to the best-fit value determined from elliptical Gaussian fitting for the data set. We also experimented with using a range of noise biases that went from 0 to 2 times the best-fit value. We found that the minimum χ^2 from this procedure was comparable to the χ^2 for the best-fit noise bias. Second, we constructed the image two-dimensional FFT, which is the visibility plane representation of the data. Third, closure quantities were computed for each model for the time and antenna sampling of the data set. Finally, reduced χ^2 was computed for closure amplitudes and closure phases for each model and each data set.

In addition to jet models, we also created a model image for an elliptical Gaussian that represents the best-fit Gaussian from Bower et al. (2004). The reduced $\chi^2 = 1.9$ from this fit is the baseline result that jet models must meet or surpass in order to remain viable.

To demonstrate the ability of our method to discriminate between models, we substituted the closure quantities from the data with closure quantities derived from model 41 in three different position angles (90, 120, and 180 degrees). We then compared the substituted closure quantities with closure quantities from all models and position angles (Figure 4). We computed the results for three different values of the noise bias. These results show that we can differentiate between position angles and models in the case of high signal-to-noise ratios (SNR).

We also considered whether there are systematic differences in the model χ^2 between different data sets (Figure 5). Seven of nine data sets are essentially consistent with each other. Data set BB130C shows a flat χ^2 as a function of position angle. This is consistent with larger than average noise (Figure 4), which was also seen in poor limits from the Gaussian fitting (Bower et al. 2004). Data set BS055C

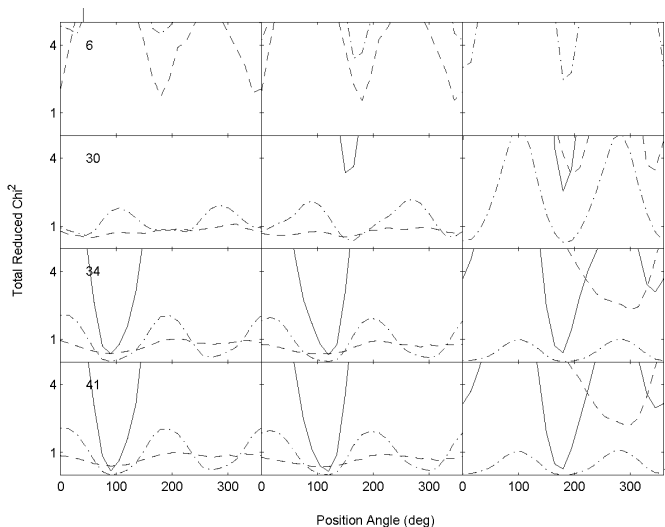


Figure 4. Total χ^2_{ν} as a function of position angle for models 6, 30, 34, and 41 for the case where the data is replaced with closure quantities calculated from model 41 in position angle 90 deg (left column), 120 deg (middle column), and 180 deg (right column). Model closure quantities were computed for three different estimates of the noise, with the solid line representing the least noise, the dot-dashed line the middle case, and the dashed line the most noise.

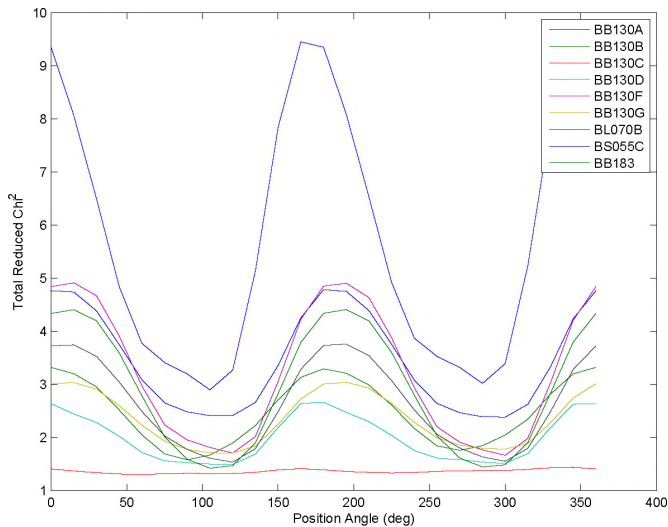


Figure 5. Total χ^2_{ν} as a function of position angle for model 41 showing each radio data set individually.

shows a similar profile in χ^2_{ν} versus position angle but significantly larger values than average. This suggests that we may have underestimated the noise for this experiment. We have therefore dropped these two outlier experiments from all further modeling results.

5 RESULTS

In Figure 6 we show all of the model images used in the analysis. In Figure 7, 8, and 9 we show the closure phase, closure amplitude, and total χ^2_{ν} as a function of position

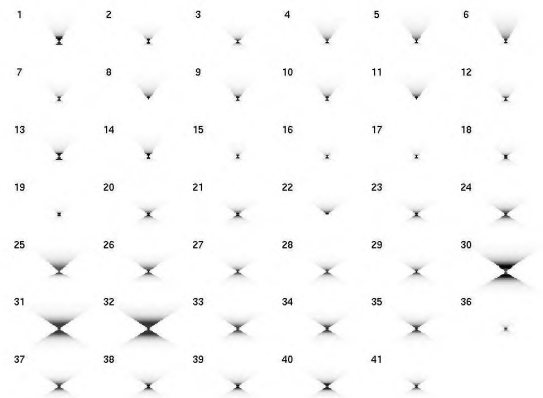


Figure 6. Images of all models prior to convolution with the scattering ellipse, with a linear stretch. The scale for each image is 1 milliarcsecond.

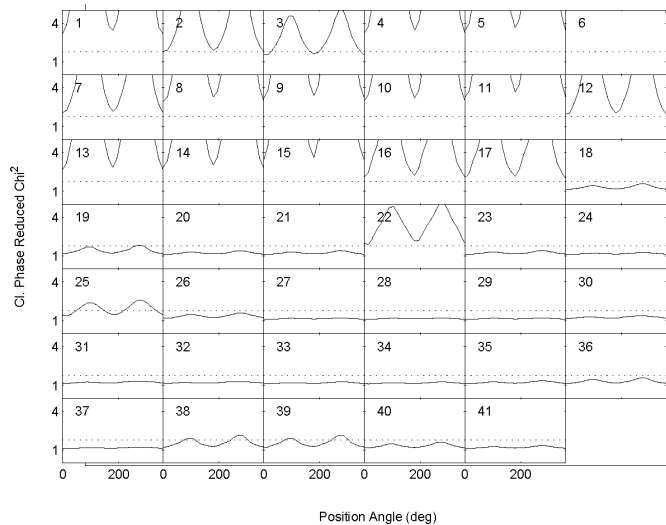


Figure 7. Closure phase χ^2_{ν} as a function of position angle for all models. The dotted line represents the reduced χ^2 for the best-fit Gaussian model.

angle for each of the models. In order to see details for the best-fitting models, we plot χ^2_{ν} only on a scale of 0 to 5. For several models, $\chi^2_{\nu} > 5$; thus where no curve is present, the model is already strongly rejected.

For a number of models, the minimum χ^2_{ν} is less than or comparable to the best-fit Gaussian model. For all cases presented here, χ^2_{ν} never achieves a significantly smaller value than the best-fit Gaussian model, which would allow unequivocal rejection of that model in favor of a jet model. Instead, these results demonstrate that we can adequately but not uniquely model the data as a bipolar, relativistic jet. This result alone shows that jets in Sgr A* cannot be ruled out on the basis of their being unresolved.

We see that most of the deviations in χ^2_{ν} as a function of position angle are visible in the closure amplitude. For many models, the closure phase χ^2_{ν} is independent of position angle and is comparable to the value from Gaussian fitting.

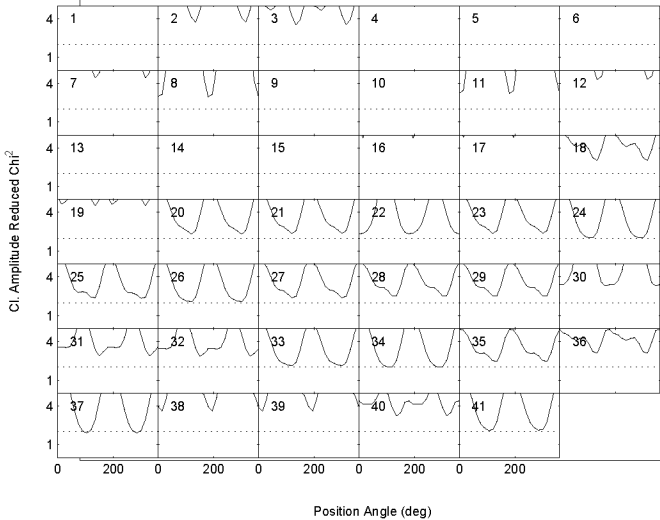


Figure 8. Closure amplitude χ^2_{cl} as a function of position angle for all models. The dotted line represents the reduced χ^2 for the best-fit Gaussian model.

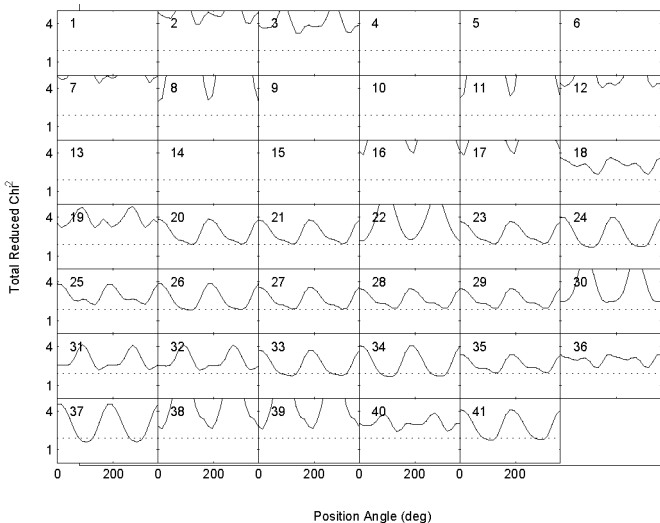


Figure 9. Total χ^2_{cl} as a function of position angle for all models. The dotted line represents the reduced χ^2 for the best-fit Gaussian model.

The closure phase results indicate that any deviations from axisymmetry in the source image are very small. The dominant role of the closure amplitude in variations with position angle is indicative of sensitivity to the size of the source in a given direction.

In the East-West direction ($90/270^\circ$), we have the best size determination because of the better resolution of the telescope in this direction. One can think of this as the data having smaller “error bars” around these angles. On the other hand, the scattering angle is largest, so asymmetries and extended components may be more obscured. In the North-South directions, the resolution is worse by a factor of ~ 3 . Thus, minima in χ^2 at 0, 180 and 360 in several models are not significant. In these cases the overall fit is very bad (as can be seen in the regions of better resolution around $90/270^\circ$) and the dips represent instead

regions where our data are the least constraining. However in several models we see minima which are clearly offset from $90/270^\circ$, such as model 41 where the minimum occurs at $\sim 105^\circ$ (this can be most easily seen in Fig. 12). The peaks seen at $0/180/360^\circ$ suggest that even with the poorest resolution, the asymmetry is too great to be consistent with those directions. The fact that the model is minimized at an angle where our ability to constrain the asymmetry is greater is suggestive, and its total χ^2 is in fact slightly lower than the best-fit Gaussian value. However, it is far too preliminary to claim a detection of a preferred position angle. These results do suggest, however, that with better resolution, especially in the N-S direction, the position angle of a jet may be constrained, particularly during flaring states. Furthermore, many position angles are clearly ruled out, never achieving close to minimum χ^2 for any spectrally consistent model.

In Figs. 10–14, we show “scatter plots” of the minimum χ^2 from Fig. 9 associated with some model parameters, for the 30 quiescent models only. The size and darkness of the circle/ellipse are inversely proportional to the χ^2 , i.e, large and black circles/ellipses are the best fits while lighter, smaller regions are not. The two data sets which are clearly discrepant from the others as discussed above, BB130C and BS055C, are not included.

Fig. 10 demonstrates the clear selection of compact jets (whose smallest scale is the nozzle radius r_0) and high inclination angles. A much more stringent constraint than the spectrum alone is the combined effect of these two parameters on the jet profile. While any compact nozzle less than several r_g , or inclination above $\sim 75^\circ$, is acceptable spectrally, the high level of symmetry required by the VLBI data strongly favors the most compact jets which are the most beamed out of the line of sight. Because the jets are mildly accelerating, the beaming-induced “dimming” increases along the jet axes, thus emphasizing the less elongated nozzle regions. These results are also a reassuring confirmation because it would be surprising and somewhat alarming if the jets were so misaligned as to be pointing significantly towards the Galactic plane in which we roughly sit. Fig 11 also compares two geometrical parameters, this time the position angle on the sky versus the inclination angle. The best fit jet is therefore almost perpendicular to us, with a position angle on the sky of $\sim 105^\circ$. Fig. 12 shows the clear peak in $1/\chi^2$ at this angle.

Fig. 13 gives an example of how the additional morphology comparisons can also help constrain internal jet parameters such as the equipartition of energy and electron temperature. While the overall range of spectrally-allowed temperatures spans a decade in temperature, the upper range clearly does not provide a compact enough jet profile. The equipartition parameter however is best constrained by the spectral fitting, which has already selected a rather narrow range. Values > 1 are magnetically dominated.

Finally in Fig. 14 we show that some parameter degeneracies clearly remain despite our new approach. Here we plot the electron temperature against the jet normalization parameter N_j . A clear range of acceptable values exists in both parameters, demonstrating for instance how a higher temperature electron distribution can compensate for lower power because of its more energetic emission. This can be

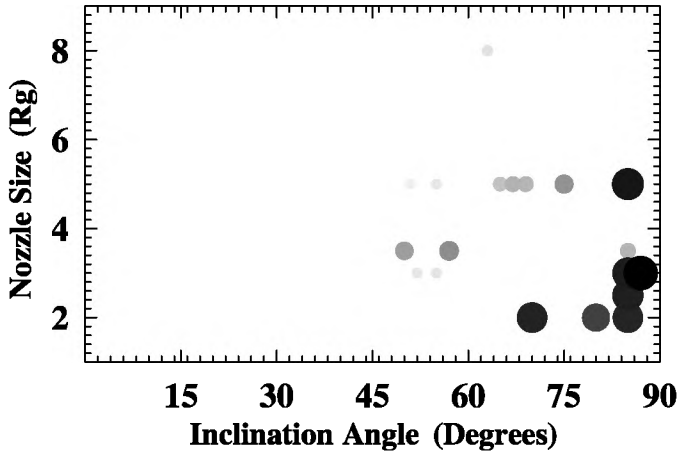


Figure 10. For each of the 30 quiescent models, we plot the minimum χ^2 in PA from Fig. 9 for the indicated nozzle radius r_0 and inclination angle. The radius and greyscale (from white to black) are linear in $1/\chi^2$, and smaller χ^2 (larger circle) fits are plotted last. The largest, darkest circles have $\chi_{\min}^2 \sim 1.5$.

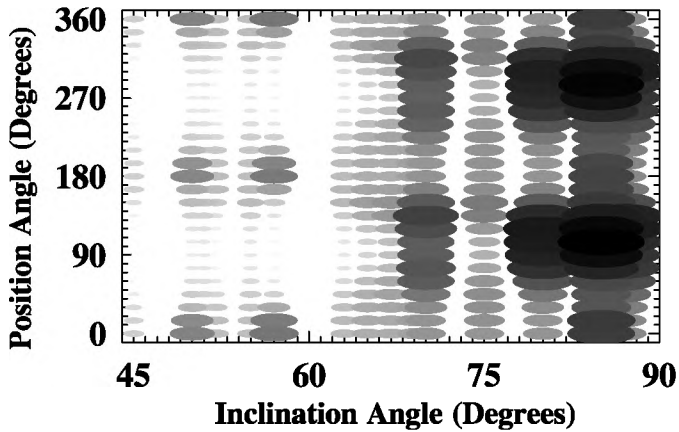


Figure 11. Color scale the same as Fig. 10, with symbols now ellipses (axes scaled linearly in $1/\chi^2$) to better illustrate the parameter space, showing χ^2 as a function of model PA and inclination angle.

understood from the critical synchrotron frequency relationship $\nu_s \propto B\gamma_e^2$, where $B^2 \propto N_j$ and $\gamma_e \propto T_e$.

6 DISCUSSION AND CONCLUSIONS

The most important conclusion of this paper is that a jet model, with reasonable physical assumptions about its geometry and internal physics, is capable of explaining the radio through IR (and higher, during flares) spectrum of Sgr A* and *not be visible at all to us as an object with jet-like morphology!* Aside from the overall low jet power, the lack of significant particle acceleration implied by Sgr A*'s IR spectrum would predict extremely compact jet profiles. Our results demonstrate that the lack of an imaged jet in Sgr A* is not necessarily due to any absence, but rather stems from a very compact, weak source combined with the rather extreme scatter broadening by Galactic electrons, and limits on our spatial resolution, especially in the N-S direction.

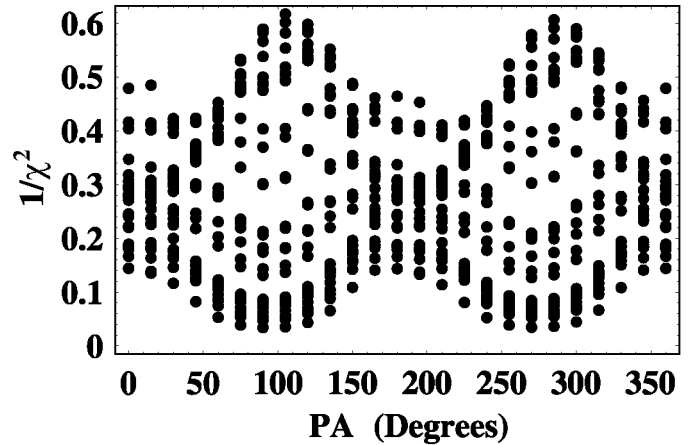


Figure 12. For all models, $1/\chi^2$ as a function of jet PA. The best fit occurs for 105/285°.

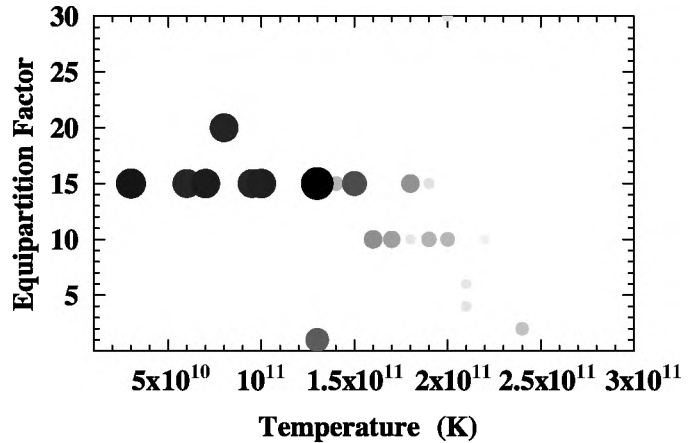


Figure 13. Same symbol definitions as Fig. 10, showing χ^2 as a function of electron temperature and equipartition parameter (between magnetic and radiating particle energy densities, with > 1 meaning magnetically dominated). These are the two most important internal rather than geometrical parameters.

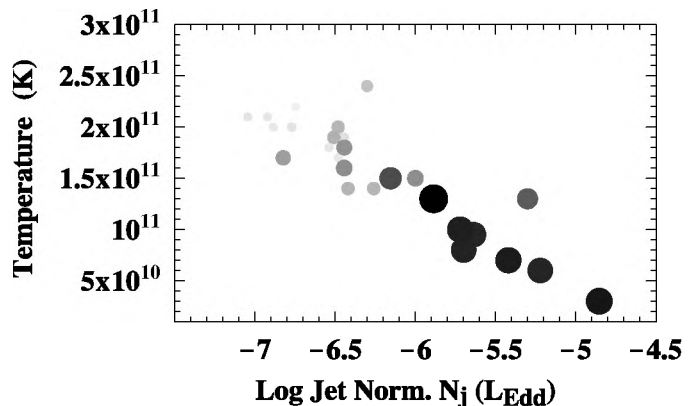


Figure 14. Same symbol definitions as Fig. 10, showing χ^2 as a function of electron temperature and jet normalizing power (related to, but slightly less than, the total power; see Appendix in Markoff et al. 2005). There is a clear relationship between these two parameters.

However, even without being able to detect a fully elongated structure, the combination of spectral fitting with constraints from comparison with VLBI morphology can significantly limit the acceptable range of parameter space for jet models of Sgr A*. Figures 10–14 visually demonstrate these new limits, which are successful despite the preliminary exploration of all parameter space.

Not altogether surprisingly, the additional inclusion of size constraints from VLBI places tighter limits on the model geometry. For instance, while fitting the quiescent spectrum can only limit the inclination angle to $\gtrsim 45^\circ$, the addition of VLBI data indicates a very clear preference for $\theta_i \sim 90^\circ$. Similarly, the size constraints from VLBI also narrow the range in jet nozzle size from $\lesssim 8r_g$ to $\lesssim 5r_g$ with the best fits at the smaller end. In the context of jet models, this would require jet launching to occur very close to the black hole, within the innermost stable circular orbit (ISCO) for a Schwarzschild black hole.

Size constraints also indicate that VLBI data can already begin to constrain the orientation of jets on the sky. The best fit is found over a narrow range $90 - 120^\circ$ centered at $\sim 105^\circ$, in a region where the resolution of the VLBI is good enough to begin discerning the asymmetry. The preferred PA is interesting, in that it could be related to the average position angle of the electromagnetic fields and thus give further clues about jet geometry. Recent observations of variable linear polarization by Bower et al. (2005) and Marrone et al. (2006a) observed PA changes of $30^\circ - 60^\circ$ over timescales of days to months. Infrared measurements of the polarization during flares also show significant variability (Trippe et al. 2007). The variability is most likely intrinsic, although there may be a favored or mean intrinsic polarization PA in the various wavelengths, though currently they do not seem to agree with each other. Confirming both angles may ultimately provide important information about the helicity of the magnetic field threading the jets, or near the black hole.

In addition, Figs. 7-9 clearly indicate a dramatic difference in the goodness-of-fit between quiescent and flaring models for Sgr A*. This is because the mechanisms involved in creating the flares (Markoff et al. 2001; Liu & Melia 2002; Yuan et al. 2003) are either heating or accelerating the radiating particles, which alters the optical depth and changes the jet profile on the sky. Our results strongly argue for further simultaneous X-ray and VLBI (eventually preferentially in the millimeter regime) monitoring of Sgr A*, where these methods can strongly limit the contributions of acceleration and heating, respectively.

In conclusion, we find that the combination of broadband spectral and morphological constraints gives encouraging and interesting limits on jet models (or any model) which cannot be obtained by spectral fitting alone. In particular, the current difficulty in constraining the high-energy contribution of the jets because of the dominant quiescent thermal X-ray emission highlights the need for new approaches. Including constraints from VLBI images offers a powerful method to break the current degeneracy in theoretical models for Sgr A*'s emission, as well as better constraint individual models themselves.

At 43 GHz and below, the key outstanding problem is to measure the two dimensional structure of Sgr A*. This requires a careful selection of North-South baselines that are

sensitive to structure on the scale of a few hundred micro-arcseconds. However, it is important to note that electron scattering still acts to symmetrize the data at 43 GHz, thus mm/submm VLBI could be even more revealing for these types of studies. The advantage may, however, be offset by the fact that higher frequencies probe even smaller scales in the jets, which would be predicted to be as symmetric as an accretion flow. On the other hand, mm/submm VLBI will bring us to scales comparable to those probed by the IR/X-ray flares. While this will allow us to better observe simultaneous flares in all three frequency bands, it also raises the question of how to distinguish the base region of a jet from an accretion flow. By identifying structural changes in morphology with spectral changes in a flare, the approach presented in this paper will be able to constrain the geometry, particle distributions and emission mechanisms contributing to the flares.

Finally we emphasize that the results presented here do not include modifications due to general relativistic effects near the black hole. For the current resolutions this may not be critical, but as we probe closer to the innermost regions with higher frequencies, this clearly needs to be taken into account (e.g. Falcke et al. 2000; Broderick & Loeb 2005).

ACKNOWLEDGMENTS

We would like to thank Michael Wise for help with the scripts for producing FITs images from the calculations. H.F. would like to thank the Miller Institute for hosting his Visiting Miller Professorship at the Astronomy Department of UC Berkeley, during which significant progress on this paper was made.

REFERENCES

- Aitken D. K., Greaves J., Chrysostomou A., Jenness T., Holland W., Hough J. H., Pierce-Price D., Richer J., 2000, *ApJ*, 534, L173
- An T., Goss W. M., Zhao J.-H., Hong X. Y., Roy S., Rao A. P., Shen Z.-Q., 2005, *ApJ*, in press, (astro-ph/0503527)
- Backer D. C., Sramek R. A., 1999, *ApJ*, 524, 805
- Baganoff F. K., 2003, *AAS/High Energy Astrophysics Division*, 7,
- Baganoff F. K., Bautz M. W., Brandt W. N., Chartas G., Feigelson E. D., Garmire G. P., Maeda Y., Morris M., Ricker G. R., Townsley L. K., Walter F., 2001, *Nature*, 413, 45
- Baganoff F. K., Maeda Y., Morris M., Bautz M. W., Brandt W. N., Burrows D. N., 2003, *ApJ*, 591, 891
- Balick B., Brown R. L., 1974, *ApJ*, 194, 265
- Bélanger G., Goldwurm A., Melia F., Ferrando P., Grosso N., Porquet D., Warwick R., Yusef-Zadeh F., 2005, *ApJ*, 635, 1095
- Bietenholz M. F., Bartel N., Rupen M. P., 2000, *ApJ*, 532, 895
- Blandford R. D., Königl A., 1979, *ApJ*, 232, 34
- Bower G. C., Falcke H., Herrnstein R. M., Zhao J., Goss W. M., Backer D. C., 2004, *Science*, 304, 704
- Bower G. C., Falcke H., Mellon R. R., 2002, *ApJ*, 578, L103

- Bower G. C., Falcke H., Wright M. C., Backer D. C., 2005, *ApJ*, 618, L29
- Bower G. C., Goss W. M., Falcke H., Backer D. C., Lithwick Y., 2006, *ApJ*, 648, L127
- Bower G. C., Wright M. C. H., Falcke H., Backer D. C., 2003, *ApJ*, 588, 331
- Broderick A. E., Loeb A., 2005, *MNRAS*, 363, 353
- Brunthaler A., Bower G. C., Falcke H., 2006, *A&A*, 451, 845
- Brunthaler A., Bower G. C., Falcke H., Mellon R. R., 2001, *ApJ*, 560, L123
- Corbel S., Nowak M., Fender R. P., Tzioumis A. K., Markoff S., 2003, *A&A*, 400, 1007
- Eckart A., Baganoff F., Morris M., Bautz M. W., Brandt W., Garmire G., Genzel R., Ott T., Ricker G., Straubmeier C., Viehmann T., Schödel R., 2004, *A&A*
- Falcke H., 1996, *ApJ*, 464, L67
- Falcke H., Biermann P. L., 1995, *A&A*, 293, 665
- Falcke H., Biermann P. L., 1999, *A&A*, 342, 49
- Falcke H., Körding E., Markoff S., 2004, *A&A*, 414, 895
- Falcke H., Markoff S., 2000, *A&A*, 362, 113
- Falcke H., Melia F., 1997, *ApJ*, 479, 740
- Falcke H., Melia F., Agol E., 2000, *ApJ*, 528, L13
- Fender R., Corbel S., Tzioumis T., McIntyre V., Campbell-Wilson D., Nowak M., Sood R., Hunstead R., Harmon A., Durouchoux P., Heindl W., 1999, *ApJ*, 519, L165
- Fender R. P., Gallo E., Jonker P. G., 2003, *MNRAS*, 343, L99
- Gallo E., Fender R. P., Miller-Jones J. C. A., Merloni A., Jonker P. G., Heinz S., Maccarone T. J., van der Klis M., 2006, *MNRAS*, 370, 1351
- Gallo E., Fender R. P., Pooley G. G., 2003, *MNRAS*, 344, 60
- Genzel R., Schödel R., Ott T., Eckart A., Alexander T., Lacombe F., Rouan D., Aschenbach B., 2003, *Nat.*, 425, 934
- Ghez A. M., Morris M., Becklin E. E., Tanner A., Kremenek T., 2000, *Nat.*, 407, 349
- Ghez A. M., Wright S. A., Matthews K., Thompson D., Le Mignant D., Tanner A., Hornstein S. D., Morris M., Becklin E. E., Soifer B. T., 2004, *ApJ*, 601, L159
- Ho L. C., 1999, *ApJ*, 516, 672
- Körding E., Falcke H., Corbel S., 2006, *A&A*, 456, 439
- Lind K. R., Blandford R. D., 1985, *ApJ*, 295, 358
- Liu S., Melia F., 2002, *ApJ*, 566, L77
- Macquart J.-P., Bower G. C., Wright M. C. H., Backer D. C., Falcke H., 2006, *ApJ*, 646, L111
- Markoff S., Falcke H., Fender R., 2001, *A&A*, 372, L25
- Markoff S., Falcke H., Yuan F., Biermann P. L., 2001, *A&A*, 379, L13
- Markoff S., Nowak M., Corbel S., Fender R., Falcke H., 2003, *A&A*, 397, 645
- Markoff S., Nowak M. A., Wilms J., 2005, *ApJ*
- Marrone D. P., Moran J. M., Zhao J., Rao R., 2006a, *ApJ*
- Marrone D. P., Moran J. M., Zhao J.-H., Rao R., 2006b, *ApJ*, 640, 308
- Melia F., 1992, *ApJ*, 387, L25
- Melia F., Falcke H., 2001, *ARA&A*, 39, 309
- Merloni A., Heinz S., di Matteo T., 2003, *MNRAS*, 345, 1057
- Merloni A., Körding E., Heinz S., Markoff S., Di Matteo T., Falcke H., 2006, *New Astronomy*, 11, 567
- Migliari S., Tomsick J. A., Markoff S., Kalemci E., Bailyn C., Buxton M., Corbel S., Fender R. P., Kaaret P., 2007, *ApJ*
- Nagar N. M., Falcke H., Wilson A. S., 2005, *A&A*, 435, 521
- Nagar N. M., Falcke H., Wilson A. S., Ulvestad J. S., 2002, *A&A*, 392, 53
- Narayan R., Mahadevan R., Grindlay J. E., Popham R. G., Gammie C., 1998, *ApJ*, 492, 554
- Nord M. E., Lazio T. J. W., Kassim N. E., Goss W. M., Duric N., 2004, *ApJ*, 601, L51
- Quataert E., 2002, *ApJ*, 575, 855
- Reid M. J., Menten K. M., Genzel R., Ott T., Schödel R., Eckart A., 2003, *ApJ*, 587, 208
- Roy S., Pramesh Rao A., 2004, *MNRAS*, 349, L25
- Schödel R., Ott T., Genzel R., Eckart A., Mouawad N., Alexander T., 2003, *ApJ*, 596, 1015
- Shakura N. I., Sunyaev R. A., 1973, *A&A*, 24, 337
- Shen Z.-Q., Lo K. Y., Liang M.-C., Ho P. T. P., Zhao J.-H., 2005, *Nat.*, 438, 62
- Trippe S., Paumard T., Ott T., Gillessen S., Eisenhauer F., Martins F., Genzel R., 2007, *MNRAS*, 375, 764
- Yuan F., Markoff S., Falcke H., 2002, *A&A*, 383, 854
- Yuan F., Markoff S., Falcke H., Biermann P. L., 2002, *A&A*, 391, 139
- Yuan F., Quataert E., Narayan R., 2003, *ApJ*, 598, 301
- Yuan F., Shen Z.-Q., Huang L., 2006, *ApJ*, 642, L45
- Yusef-Zadeh F., Roberts D., Wardle M., Heinke C. O., Bower G. C., 2006, *ApJ*, 650, 189